Article

Solvent Regeneration by Thermopervaporation in Subsea Natural Gas Dehydration: An Experimental and Simulation Study

Mahdi Ahmadi, Luca Ansaloni, Magne Hillestad,* and Liyuan Deng*

Read Online

ACCESS | Metrics & More | Article Recommendations | SI Supporting Information

ABSTRACT: An in-house designed membrane process suitable for subsea natural gas dehydration was studied. The use of a membrane absorber together with a thermopervaporation (TPV) unit for solvent regeneration in a closed loop enables the effective and clean production of high-pressure natural gas close to the wellhead. This process avoids the continuous chemical injection for preventing hydrate formation in natural gas pipelines. The regeneration of the absorbent agent (triethylene glycol (TEG)) by TPV in the closed loop is highly energy-efficient, owing to the unlimited free cooling energy from the cold subsea water. In this work, the performance of membranes in TPV for TEG regeneration was evaluated experimentally for the first time. Morphological and permeation characterizations of an AF2400 thin-film composite membrane were carried out, and high separation factors outperforming the vapor−liquid equilibrium (VLE) were obtained for the solutions containing various water contents at feed temperatures ranging from 30 to 70 °C. The highest values of a separation factor (128,000) and a permeability (2380 (Barrer)) were obtained for the TEG solution containing 30 wt % water at 30 °C, while the highest water flux (468 (g/m^2·h)) was reached at 70 °C. Moreover, the concentration polarization phenomenon induced by the temperature gradient was revealed in the membrane's vicinity of the feed channel. A 3D computational fluid dynamics simulation was performed over the entire module to correct the driving force for a more precise assessment of the membrane permeance. The temperature and concentration profiles in the membrane module domains were explored, and a good agreement with experimental data was obtained.
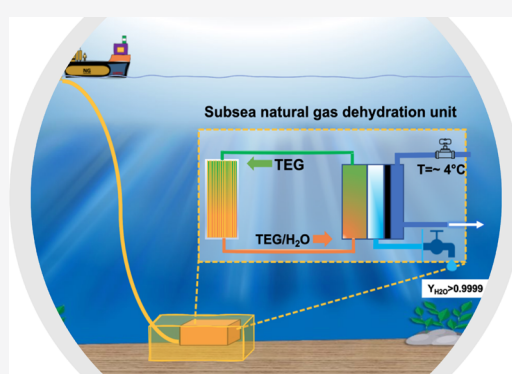
1. INTRODUCTION

The lack of easily accessible natural gas resources and the advancement of new technologies for cheaper exploration have motivated the petroleum industries to exploit more underwater natural gas reservoirs and subsea gas treatment.[1−4] The pipeline blockage and corrosion of installations caused by impurities in natural gas are the main issues in gas transportation.[4,5] Water vapor is blamed for being the chief culprit in fast aging of the installation and hydrate formation, blocking high-pressure pipelines. Much effort is required to bring down the water content in the high-pressure gas stream to meet the pipeline specifications and prevent the flow assurance problems. Currently, available dehydration technologies include adsorption (with solid desiccants such as zeolites), absorption (with liquid desiccants such as glycols), condensation, and membrane separation.[6] Absorption with glycols is the most frequently used technology in which the lean glycol stream absorbs water vapor in an absorption column and then liberates it in a regeneration unit at higher temperature.[7] Among the commercially available glycols, triethylene glycol (TEG) has been widely consumed in the oil and gas industries as the conventional absorbent and received the universal acceptance as the cost-effective and economical liquid desiccant.[8] Monoethylene glycol (MEG) and diethylene glycol (DEG) were also commonly used in

dehydration processes.[9] Compared to MEG and DEG, TEG has proven superior performance with lower vapor pressure, lower operating costs, and higher hygroscopic properties.[8] Additionally, the energy consumption of the thermal regeneration of TEG is lower than those of MEG and DEG.

However, several critical aspects and limitations undermine the bargaining power of the traditional absorption−desorption units in the design of subsea processes. For instance, subsea equipment requires a technology with small footprints, easy installation, fewer moving parts, and compact design and modularity,[1] which are the features missing in traditional absorption or desorption units. Surprisingly, all these are, in fact, the main advantages of membrane-based gas separation processes, enabling membrane technology to have the upper hand in competing with the conventional absorption process in subsea process design. Moreover, membrane processes usually
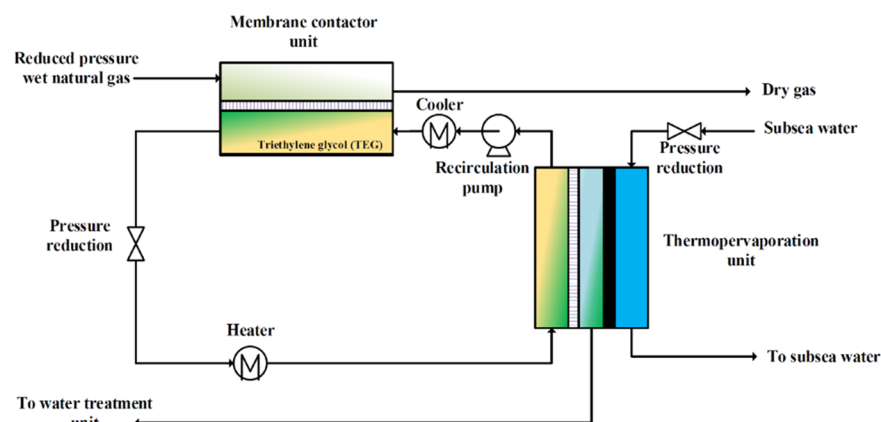
Figure 1. Proposed subsea natural gas dehydration process diagram.[10]

need little maintenance and have less chemical emission than the conventional technologies; hence, they are more advantageous for subsea or unmanned offshore factories.

The SUBPRO Research Centre (Norway) has recently developed a conceptual closed-loop membrane process for subsea natural gas dehydration (Figure 1).[10] The process is a hybrid absorption—membrane process with combined benefits of high compactness/modularity of the membrane process and the high selectivity of the absorption using a TEG absorbent agent. The closed loop also leads to less TEG emission and methane loss. The TEG and methane loss are the main criteria for cleaner production of dehydrated natural gas streams in unmanned subsea facilities. The noted closed loop includes a membrane contactor unit operating at high pressure to absorb water from natural gas and a thermopervaporation (TPV) unit operating at low pressure for the regeneration of the absorbents. The feed stream has a high-pressure close to the wellhead pressure and is saturated with water vapor at the temperature of the gas stream, which provides the highest driving force for water absorption, while the cold subsea water provides the cooling energy for the TEG regeneration in TPV. The free source of low-temperature subsea water makes the thermopervaporation unit an economically sensible and efficient method for TEG regeneration.

The present work focuses on the TPV step in the proposed closed-loop process designed for subsea dehydration of natural gas through the experimental study on the separation performance of TPV and by modeling and simulating the momentum, heat, and mass transfer in the module.

Pervaporation has been widely applied to liquid—liquid/ vapor—liquid separation with an emphasis on alcohol/water systems,[11−21] bio-oil dehydration,[22] hazardous substances and organic solvent removal from water,[23,24] solvent regeneration from complex mixtures,[25] isomer separation,[26] and glycol dehydration.[27−32] The pervaporation process benefits from the membrane selectivity in addition to the vapor—liquid equilibrium selectivity. Only minor components (usually more volatile) of the mixture evaporate and transfer to the permeate side of the membrane; much less energy consumption is required compared with VLE-based separation technologies.[33] The driving force for water transport in pervaporation, i.e., the chemical potential difference (water vapor partial pressure in this case), is usually supplied using a continuous vacuum pump or sweep gas. The transport mechanism in pervaporation through polymeric membranes is the standard "solution-diffusion" mechanism, where a nonporous selective membrane

is used.[34] Although the process requires latent heat for evaporation of a liquid mixture, pervaporation is recommended as an energy-saving process compared to distillation operation.[30] For subsea operation, however, the main disadvantage of pervaporation is the need for continuous vacuum, which can hardly be applied to subsea where the maintenance of vacuum at the required level is not economically viable.[35]

If the chemical potential difference across the membrane in pervaporation is induced by a temperature gradient across the membrane, the process is then named thermally driven pervaporation or thermopervaporation (TPV).[36,37] The term "thermopervaporation" was proposed by Aptel et al. for the first time.[37] In their work, a PTFE-PVP membrane was used in the TPV process for the separation of organic/organic and water/ organic compounds by fractionating the positive azeotrope. Later, Spitzen investigated the application of thermopervaporation with two different configurations, i.e., direct contact and air-gap thermopervaporation.[29] In direct contact thermopervaporation, the membrane is in direct contact with the cold liquid from the downstream side, while in the air-gap thermopervaporation, an air gap is placed between the membrane interface and a condensing plate that is kept at low temperature using a cooling liquid. The permeating vapors are condensed on the cooling plate, and subsequently, the droplets are removed from the air gap by gravity. For subsea operation, the use of TPV offers a more useful design option than continuous vacuum pervaporation. The subsea cold water as the free source of cooling energy can be used to generate the mass transfer driving force induced by a temperature gradient.

Concerning glycol regeneration, evaporation (e.g., distillation) is found to be a suitable technology for solutions containing less than 70 wt % glycol.[38] Beyond this value (above 70%), energy demands increase remarkably. Membrane pervaporation has, therefore, been of great interest as an alternative for energy-intensive distillation processes for glycol solutions containing glycol of above 70 wt %.[38] In our previous work on TPV modeling,[39] experimental data for the model validation was limited only to the membrane permeation properties obtained from vacuum pervaporation testing using a Teflon AF2400 membrane. Concerning the TEG dehydration in thermopervaporation, experimental work has seldom been reported. Golubev et al.[40] have recently reported experimental permeation data for several hydrophilic and hydrophobic commercial membranes in an air-gap thermopervaporation system with a porous condenser. However, no separation factor was reported in their study.

There are also several other works focusing on vacuum pervaporation, but they were for dehydration of ethylene glycol with the major attention on membrane material development. Poly(acrylic acid) (PAA),[41,42] poly(vinyl alcohol) (PVA),[43−46] polybenzimidazole,[32,38] and chitosan[41,42,47] have been the frequently reported membranes used for glycol regeneration, which are all hydrophilic. These polymeric membranes suffer from the lack of mechanical strength and chemical stability due to swelling in contact with aqueous solutions. Some efforts have been spent on cross-linking the membranes to improve their mechanical strength when swelling, but then the permeability and flux were compromised.[27,48]

The compatibility and durability of the polymer in contact with TEG are critical in membrane material selection to ensure that the membrane is not swollen in contact with TEG and preserves its performance under long-term subsea operation. Thus, the present work experimentally assesses the performance of a TPV module using a Teflon AF2400 membrane, as Teflon AF2400 has been extensively examined by compatibility tests with TEG regarding the TEG uptake; excellent mechanical and chemical stability that was reported leads to minimizing the TEG emission.[39] Teflon AF2400 is a copolymer consisting of tetrafluoro-ethylene (TFE) and 2,2-bis(trifluoromethyl)-4,5-difluoro-1,3-dioxole (BDD) with a molar ratio of 13−87% and has a glass transition temperature of 240 °C and a large free volume of about 33%.[49−52] TeflonAF2400 has been frequently reported for gas separation applications.[5,39,53−59] Despite the hydrophobic nature of the glassy Teflon AF2400, the polymer ensures high gas flux and separation factors, possibly due to its high free volume and high molecular chain rigidity, respectively.[60]

Several modeling and simulation studies have been carried out on pervaporation membrane modules for various applications in which the primary focus of the modeling strategies was resistance-in-series mass transfer models in the membrane phase.[46] Considering the TPV process, however, the importance of non-isothermal modeling stems from the fact that the temperature profile plays a critical role in transporting components through the membrane and air gap. The temperature profile in the air gap is correlated with the concentration of the component in the air gap. Therefore, an accurate model could be useful to be integrated with the experimental study for better characterization of the membrane performance. The available modeling studies were performed over 2D domains; Koter et al.[61] applied the resistance-in-series model for the 2D heat and mass transfer models to study the temperature and concentration profiles and process performance in the thermopervaporation process for an ethanol−water mixture. The model was suggested for the temperature and concentration profile in the air gap. The highest temperature drop was reported to occur in the air gap, where the temperature gradient across the air gap was 2 times higher than that of the membrane. In a similar work, Borisov et al.[62] explored the temperature and concentration profile in the air gap for a binary mixture of water−butanol in a dense poly(1-trimethylsilyl-1-propyne) (PTMSP) membrane. The empirical model was found to be in good agreement with experimental data, showing a dependency of the permeate flux on the temperature profile. The coolant's optimum temperature was obtained where the flux and separation factor enhanced as the feed temperature increases. Dalane et al.[39] conducted a simulation study on the performance of the Teflon AF2400 membrane in the thermopervaporation process for subsea dehydration of the TEG. The modeling study

was a 2D resistance-in-series simulation where the membrane properties from a vacuum pervaporation were used to predict the performance of TPV. It was concluded that the separation performance is highly affected by the geometry and temperature profile in the air gap.

In the present work, an optimized TPV membrane module using Teflon AF2400/PP composite membranes and a TPV testing system with automatic control and data collection were in-house designed and installed. New experimental methods and protocols for the TPV performance evaluation were established, and the TPV membrane modules and processes were experimentally studied for the first time. Moreover, an intensively validated 3D simulation over the entire module using computational fluid dynamics (CFD) with the finite element method (FEM) in COMSOL Multiphysics 5.5 was performed to investigate the average temperature of the air gap for a more accurate calculation of water permeability. The models have also been extended to explore the concentration gradient in the air gap and feed channel, to determine the "concentration polarization" phenomenon in the feed solution, and to study the effects of the temperature and velocity profiles in the entire membrane module.

2. EXPERIMENTS AND METHODS

2.1. Materials. Perfluorinated Teflon AF2400 was supplied by Chemours (the Netherlands). A perfluorohexane (FC-72) solvent was purchased from Kemi Intressen AB (Sweden). Triethylene Glycol ReagentPlus 99% (TEG) and triethylene glycol monomethyl ether 95% (TEG ME) were purchased from Sigma-Aldrich (Norway). All the chemicals were used as received with no further purification. A porous polypropylene (commercially known as PP-2400) film was kindly supplied by Celgard LLC (USA). Table 1 lists the PP-2400 porous membrane specification provided by the producer.

Table 1. PP-2400 Porous Membrane Specification, Celgard LLC (USA)

property	value
thickness	25−30 (μm)
porosity	41%
average pore Size	0.043 (μm)

2.2. Preparation of the Teflon AF2400/Polypropylene Composite Membrane. A solution of 1 wt % Teflon AF2400 was prepared by dissolving the weighed amount of polymer resins in FC-72 and stirred overnight at ambient temperature to obtain a clear and homogeneous solution. Porous polypropylene was stretched, placed, and attached to a glass plate. The porous PP support was sealed from the edges with adhesive aluminum tape to avoid liquid penetration on the back side of the support. The 1 wt % AF2400 solution was cast on the flattened polypropylene using conventional knife casting method with an initial knife gap of ~220 μm. The membrane was instantly transferred to a preheated vacuum oven adjusted at 80 °C and isothermally dried overnight under continuous vacuum.

2.3. Membrane Characterization. A scanning electron microscopy (SEM) instrument (Hitachi TM3030 model) was employed to examine the cross-sectional morphology of the membranes and provide detailed information of the porous support structure and thickness of the dense selective layer. Three random samples of the AF2400/PP composite membranes were taken from different locations of the dried
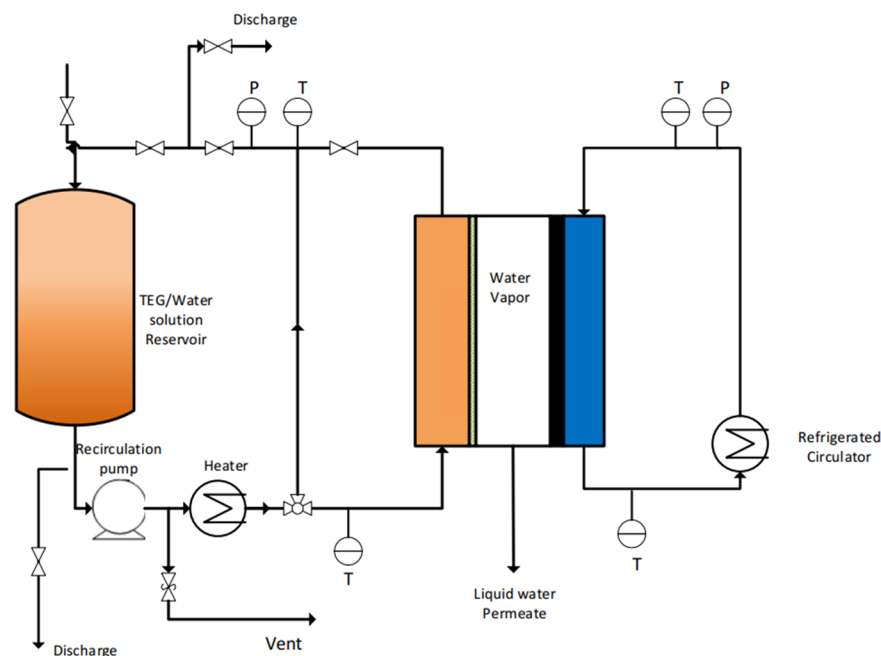
Figure 2. Thermopervaporation membrane setup.

membranes to ensure the uniformity of dense layer thickness. The samples of the as-prepared composite membrane were immersed in liquid nitrogen before making the cross-section samples. The sample surfaces were coated with gold (Au) using a Quorum Q150 ES sputter coater instrument for 120 s at 20 mA prior to the SEM imaging.

2.4. Membrane Module and Thermopervaporation Setup. The flat sheet membrane module was designed and fabricated in-house (Figure S3 in the Supporting Information). The module comprises four components, namely, feed channel, air gap, condensing plate, and cooling channel (the geometry dimensions of the module are presented in Table S2 in the Supporting Information). The feed channel and cooling channel sides were made of plexiglass to mitigate the heat transfer rate between the surrounding environment and flowing liquids. The air gap and condensing plate were made of stainless steel to enhance the thermally assisted driving force between the hot feed and cooling liquid (Figure S3c−e). The module was designed to accommodate a membrane area of 42.25 cm^2. The feed solution and cooling water flow countercurrently, parallel to the membrane, and the liquid inlet and outlet are located perpendicularly to the feed channel. The feed solution first enters a gap before flowing over effective membrane length, and then the solution flows axially over the membrane through the channels with the dimensions of $65 \times 95 \times 4$ mm^3. The dense selective layer of the composite membrane was faced to the feed solution with the membrane placed between the feed channel and air gap, supported with a metal mesh (1.0 mm thick) to prevent sagging of the membrane into the air gap. The feed solution is pumped upward to reduce the risk of bubble formation in the feed channel. The 5 mm thick air-gap framework consists of a rectangular centroid gap with a dimension of 65×65 mm^2 and 5 mm depth (including 1 mm thick mesh). A triangle channel, giving a 4 mm gap, is located downside in the air-gap framework for the removal of condensed permeated water (Figure S3c,d). The membrane module was sealed and placed vertically, and it was confined on all outer sides with natural convection at room temperature (Figure S3f,g).

The flow diagram of the TPV testing rig is presented in Figure 2. The testing rig was built in-house, and it consists of the hot side (left) and the coolant side (right) with the membrane module connecting both sides. As seen from the figure, on the feed side, a solution at specified water content was pumped using a gear pump (Izmatec BVP-Z) at a flow rate of between 150 and 200 mL/min. Prior to flowing the feed solution on the membrane, the solution was preheated using a Julabo heating bath, bypassing the membrane module and circulating overnight at a constant temperature in a closed system to obtain a stable temperature and pressure at the feed solution reservoir. Simultaneously, cooling water was supplied to the membrane module at a flow rate of about 4 L/min using a refrigerating bath set at 4 °C, which is close to the seawater temperature subsea.

The hot solution in the feed side flows upward, and the cooling water in the cooling side flows countercurrently with respect to the feed solution, as seen in the figure. Digital transmitters were employed to control and monitor the process parameters, including inlet and outlet temperatures and operating pressures. The obtained data were collected every single second using the LabView program. The average temperature of the inlet and outlet was employed to calculate fluid properties such as activity coefficient and vapor pressures. The mass flow rates of the feed and cooling flow were measured from the discharge and are listed in Table S3 in the Supporting Information together with the measured operating conditions for each experiment. The variation in the flow rate was due to the varying fluid viscosity at different feed concentrations. The permeating water condensed on the cold plate was collected from the exit triangle channel located at the underside of the membrane module. The total mass flux was measured experimentally when a steady-state condition was reached. A fresh TEG/water solution at a predetermined concentration was always used for each experiment at specified operating temperatures to reduce the effect of concentration change on the feed solution in the feed reservoir during a long-term operation. A calibrated Agilent 7820A gas chromatograph equipped with an FID detector and CP-Wax 57 CB column was

employed to detect the glycol concentration in the permeated water. TEG ME was used as an internal standard to increase the accuracy of the measurement. All samples were diluted with water to avoid the TEG carryover. In addition, samples were tested three times with GC for each experiment and some experiments were selected randomly to be tested twice to assure that the GC chromatographs are identical and not affected by carryover of testing concentrated samples.

When steady-state conditions are achieved, the total flux j (g/ m^2·h) is calculated from the following formula:

$$j = \frac{M_{\text{tot}}}{A_m t} \tag{1}$$

where M_{tot} is the total mass permeated (g) for a given time t (h) and A_m is the membrane area (m^2). The flux of the ith component is given by eq 2

$$j_i = j \times w_i \tag{2}$$

w_i is the weight fraction of component i in the permeated mass obtained from the GC analysis. The performance of the membrane material was evaluated by measuring the permeance and permeability of water component. The permeance of a composite membrane in the thermopervaporation process is calculated using eq 3, where the effect of driving force (partial pressures) is eliminated from the flux for a gas component.

$$P_{AF2400,i} = \frac{j_i}{Mw_i(x_i\gamma_i p_i^{\text{sat},f} - y_i p_T)} \tag{3}$$

$P_{AF2400,\ i}$ denotes the membrane permeance (GPU) where $1\text{GPU} = 10^{-6}\text{cm}^3$ (STP) cm^{-2} s^{-1} cmHg^{-1}, Mw_i is the molecular weight of component i (g/mol), and γ_i is the activity coefficient of the ith component in feed solution, which is calculated from the Parish model developed for the TEG/water system.[63] $p_i^{\text{sat},f}$ is the vapor pressure of the ith component in the feed solution (cmHg) obtained from the Antoine equation (for water) at average temperature of the inlet and outlet of feed solution.[64] The present work does not consider the TEG component due to the lack of information for the correlation for the low temperature vapor pressure of TEG. $y_i p_T$ is the partial pressure of component i (water) in the air gap (cmHg), which is assumed to be equal to the vapor pressure of i at the average temperature of the air gap. Contrary to the vacuum pervaporation, where the partial pressure in the permeate side is negligible, the average temperature of the air gap is of critical importance in a thermopervaporation operating at atmospheric pressure for determining the partial pressure in the permeate side. Due to the difficulty in measuring the temperature of the air gap, it was common to assume the average temperature of the condensing plate as the air-gap temperature. However, the use of the temperature value of the condensing plate as the reference for calculating the partial pressure in the air gap would oversimplify the system. It should be noted that the use of the condensing plate temperature simply ignores the concentration and temperature gradient in the air gap, leading to wrong driving forces' assumptions at higher temperatures of the feed solution. To correct the driving force, a 3D simulation was performed using a COMSOL Multiphysics CFD package (Finite element method) on the membrane module geometry. Membrane permeability (Barrer) is calculated from eq 4. l denotes the thickness of the dense layer considering negligible mass transfer resistance of the porous support, where 1 Barrer $= 10^{-10}\text{cm}^3$ (STP) cm^{-1} s^{-1} cmHg^{-1}.

$$P_{AF2400,i} = \frac{p_{AF2400,i}}{l} \tag{4}$$

The separation factor is given by eq 5 as follows

$$\beta = \frac{\left(y_{\text{H}_2\text{O}}/y_{\text{TEG}}\right)}{\left(x_{\text{H}_2\text{O}}/x_{\text{TEG}}\right)} \tag{5}$$

where $y_{\text{H}_2\text{O}}$, y_{TEG}, $x_{\text{H}_2\text{O}}$, and x_{TEG} are the mole fractions of water and TEG in the permeate and feed solution, respectively.

3. SIMULATION BASIS AND MODEL DEVELOPMENT

The momentum, heat, and mass transfer models were developed for the feed, cooling liquid, and air-gap phases and solved simultaneously to extract the average temperature of the air gap for the various experiments. The concentration profile of water in the feed channel and air gap was also obtained. The COMSOL Multiphysics package offers a thin-layer feature as the 2D boundary as the membrane interface (used in this study) with no physical thickness to reduce the computational time. This feature enables one to assign the material properties and artificial thickness of the thin boundary layer. The detailed 3D and 2D images of the domains are available and presented in the Supporting Information (Figure S4). The TEG/water feed solution contains 10 wt %, 20 wt %, 30 wt %, and 100% water. The feed exits from the upper side of the membrane module, where the cooling water enters on the other side downward. The model development for all domains, module design, mesh generation, and computational and simulation details are fully presented in part A of the Supporting Information as Model Development and Computational Details.

The physical properties of diffusion coefficients in TEG and air gap, activity coefficient, vapor pressure, viscosity, heat capacity, thermal conductivity, and enthalpy of evaporation were all entered into the software from the available models in the literature to be updated at each step size of the simulation.[39,63−66] The details of the physical properties and their function dependencies are also presented in part A in the Supporting Information.

Validation of the models and simulations was carried out by comparing the estimated values with experimental data. Three parameters of temperature, water flux, and permeability were used for verification of the simulation study with the experimental data. First, the experimentally measured temperature of the outlet of the feed solution and the cooling water are compared to the outlet-simulated temperature for the mentioned streams. The reference data and predicted data of operating conditions are presented in the Supporting Information in Table S4, in part B.

Second, water flux is a function of temperature, and a temperature-dependent model (Arrhenius model) was used as the mass transfer boundary condition of the membrane phase giving a distribution of water flux through the membrane due to the temperature distribution on the membrane surface. The flux models were obtained from the experimental data by regressing the Arrhenius model on the data for each feed concentration. The water flux model is a link between the mass transfer model and heat transfer model; therefore, a good agreement between experimentally measured flux and average simulated flux through the membrane would further validate the accuracy of the heat transfer model and temperature profile on the membrane surface. The simulation is performed mainly to obtain the average temperature of the air gap for permeability

calculations. Since in a steady-state condition, the flux through each resistance layer and membrane is equal to the overall flux, the simple and fast assumption is to use the available Arrhenius flux model to measure the average temperature of the air gap and thus the permeability, provided that the simulated average flux from the model is in good agreement with experimentally measured flux.

Third, the estimated permeabilities after correcting the driving force were also compared with the reported water permeability of Teflon AF2400 in the literature. The permeability reference data and the reported data are presented in the Supporting Information in Table S5.

4. RESULTS AND DISCUSSION

4.1. Morphological Characterization. Figure 3 displays the SEM image of the cross-section of the cast AF2400/PP
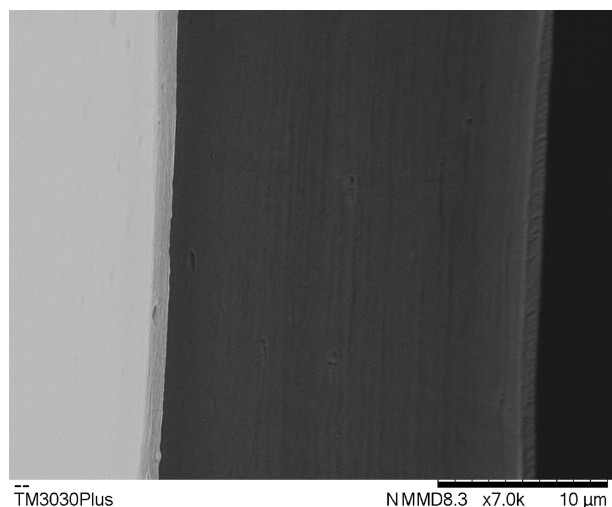
Figure 3. SEM cross-section micrograph of the AF2400/PP composite membrane.

composite membrane. The image shows the presence of the two-layer structure where a uniform, dense top layer accommodated on an about 30 μm thick porous polypropylene (PP) substrate. An average dense layer thickness of 1.6 ± 0.2 μm was measured, and it was assumed to be uniformly distributed on the membrane, which was used in this study. Due to fast evaporation of the FC-72 solvent, there is little chance for the pore penetration in the composite membrane. No pore penetration in the as-prepared membrane was observed in this work according to the resolution of the obtained SEM image. The detailed texture of the porous support can be found elsewhere,[67] where the pores are clearly seen at higher magnification. Moreover, a defect-free selective layer was obtained with uniform thickness.
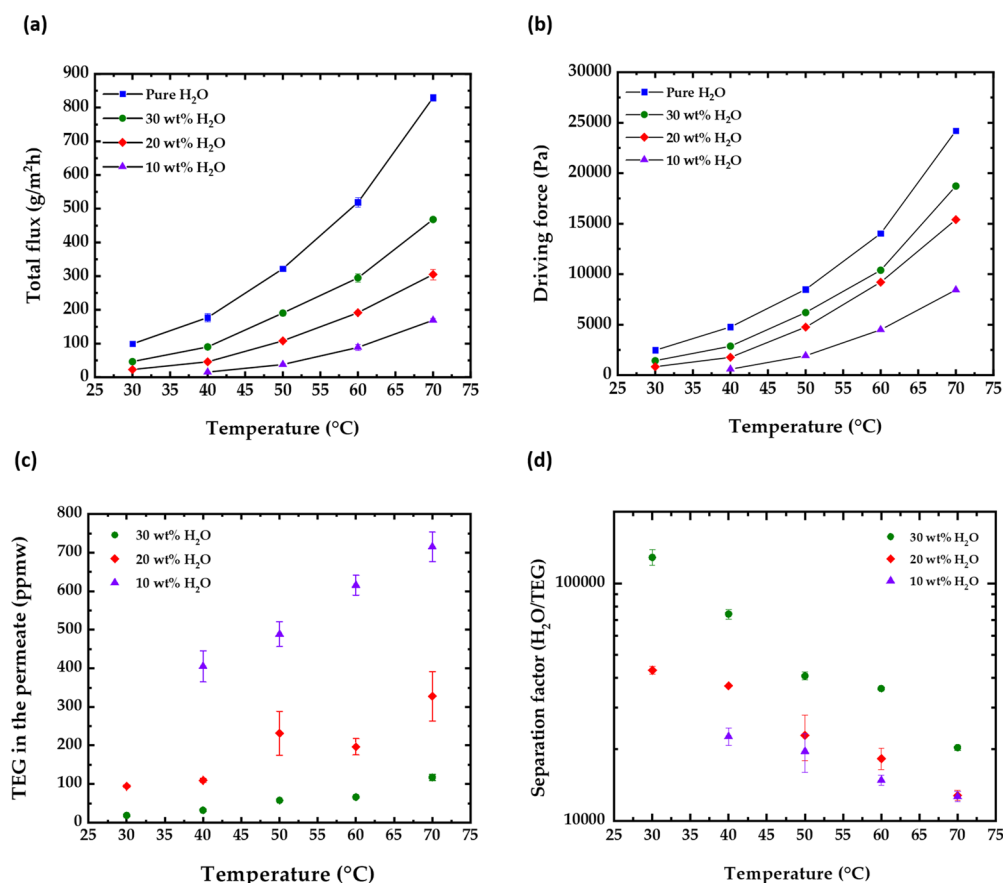
4.2. Effect of Temperature and Concentration on TPV Process Performance. The characterization of the H_2O transport through the membrane was performed for the binary mixture of H_2O/TEG at 10, 20, 30, and 100% water loadings by weight. The feed temperature ranged between 30 and 70 °C. Figure 4a presents the total permeate flux $(g/m^2 \cdot h)$ as a function of temperature at different water loadings in the feed solution. Note that the error bars are not visible as the magnitude of the error bar is smaller than the symbols. As seen from the graph, the total flux increases exponentially with the feed temperature. The lowest flux of 15.2 $(g/m^2 \cdot h)$ was measured at 40 °C for the

solution containing 10 wt % water, whereas the highest value of around 468 $(g/m^2 \cdot h)$ was measured at 70 °C for the solution containing 30 wt % water. The flux measurement for the solution containing 10 wt % water at 30 °C was lower than the detection limit; therefore, no data were obtained for this noted operating condition. The effect of temperature on the fugacity of liquid and vapor phases (driving force) is plotted as a function of temperature at various water concentrations in Figure 4b. The condensing plate temperature was used as the average temperature of the air gap for the calculations of data. As can be seen, the increment rate of flux at lower temperatures (below 50 °C) is slower for all solutions, and it sharply enhances at higher temperatures. The total water fluxes of about 100 and 830 $(g/m^2 \cdot h)$ were measured for pure water at 30 and 70 °C, respectively.

From Figure 4, an ascending trend can also be observed in the total flux with respect to water concentration in the feed solution. The general upward trend expresses the effect of water concentration on the process performance, which is due to the effect of water activity and its contribution to the driving force at the specified water concentration. The water−TEG activity (Table S6) calculations show that higher water activity is achieved at a higher temperature and water loading of the feed solution. The water activity coefficient was obtained from the Parish model.[63] With an increase in the operating feed temperature from 30 to 70 °C, the activity coefficient enhances from 0.9, 0.83, and 0.74 to 0.99, 0.97, and 0.89 for 30, 20, and 10 wt % water in the feed side, respectively.

The TEG concentration in the permeate was measured by GC analysis to examine the process selectivity, also known as the separation factor. Figure 4c presents the amount of TEG in the permeate at various temperatures. As seen from the figure, the TEG concentration in the permeate increases as the temperature increases in the feed side. The lowest TEG amount of around 18 ppmw was measured for 30 wt % water solution at the feed temperature of 30 °C, while 117 ppmw was measured at 70 °C. 3-fold and 7-fold increases in TEG concentration were measured in the permeate at 70 °C for feed concentrations of 20 wt % (327 ppmw) and 10 wt % water (715 ppmw) compared to 30 wt % water (117 ppmw), respectively.

The water/TEG separation factor of the thermopervaporation process is plotted in Figure 4d as a function of the temperature and concentration of the feed solution. The highest separation factor of above 128,000 was reached at 30 °C with 30 wt % water. As seen from Figure 4d, the separation factor shows a downward trend with rising temperature and TEG concentration on the feed side. The lowest separation factor of ∼12,600 was obtained at the highest TEG content in the feed solution at 70 °C. The downward trend with respect to the rising temperature and TEG concentration in the feed is attributed to the fact that the increase in TEG driving force is more pronounced than for water. This is possibly related to competitive sorption on the membrane matrix at higher TEG loadings and also due to the increment in TEG diffusion within the free volume of Teflon AF2400 at higher temperatures. As a comparison of the capability of the TPV process with conventional VLE-based processes, the separation factor was plotted together with the vapor−liquid-equilibrium (VLE) curves. As seen in Figure 5, the TPV process shows improved performance compared to VLE lines at all temperatures and feed concentrations studied, revealing that the membrane provides additional selectivity toward the water by posing a barrier effect toward TEG molecules. To the best of the authors' knowledge,

(a)

(b)

(c)

(d)

Figure 4. (a) Total flux, (b) driving force, (c) TEG concentration in the permeate, and (d) separation factor (H_2O/TEG) in the TPV process as a function of temperature at various concentrations in feed solutions.
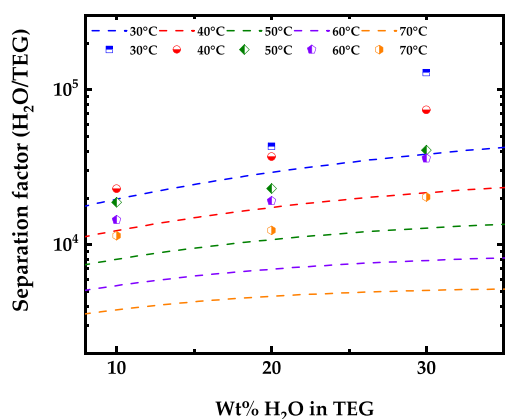
Figure 5. Separation factor of the TPV process for TEG recovery compared to VLE-based processes. The dash lines are the VLE lines obtained from Aspen plus software.

no experimental data were reported for TEG dehydration via TPV to allow for comparison with this work.

As noted in the modeling section, the temperature dependency of the total flux can be regressed and modeled in the form of the Arrhenius model.[68,69] The model parameters are presented in Table 2, where j_0 is the pre-exponential factor ($g/m^2 \cdot s$) and E_j is the apparent activation energy of the flux. The regressed model parameters are then used as a flux boundary condition of the membrane and evaporation enthalpy calculations in the air gap (as presented in detail in the modeling section in the Supporting Information). The use of the temperature-depend-

Table 2. Temperature-Dependency Parameters of the Water Flux in the Form of the Arrhenius Model

feed concentration	$\ln j_0(g/m^2 \cdot s)$	E_j (kJ/mol)	R^2
pure H_2O	15.43	47.9	99.6
30 wt % H_2O	16.72	53.1	98.3
20 wt % H_2O	17.97	58.1	98.5
10 wt % H_2O	22.53	72.9	99.7

ency model of the flux as the membrane boundary condition in the simulation study would enable one to see the concentration-temperature polarization in the feed channel. The natural logarithm of the flux versus reciprocal of temperature ($1/K$) was plotted and is displayed in Figure 6. The least-squares error method was applied to obtain the best fit where the coefficient of determinations of above 98% was obtained for all of the concentrations. Concerning the flux activation energy, the least energy barrier of 47 (kJ/mol) was estimated for pure water. The results show that the estimated values for the apparent activation energy were enhanced by 10.8, 21.3, and 52.2% for 30, 20, and 10 wt % water of the feed solution, respectively, possibly due to the competitive transport of water molecules between the membrane and the thick liquid boundary layer at higher TEG concentration.

4.3. Effect of Temperature and Concentration on Membrane Performance. The effect of temperature and concentration on the separation performance could be examined from two aspects: the process performance and membrane material performance.[70] The effect of temperature and concentration on the process performance is associated with
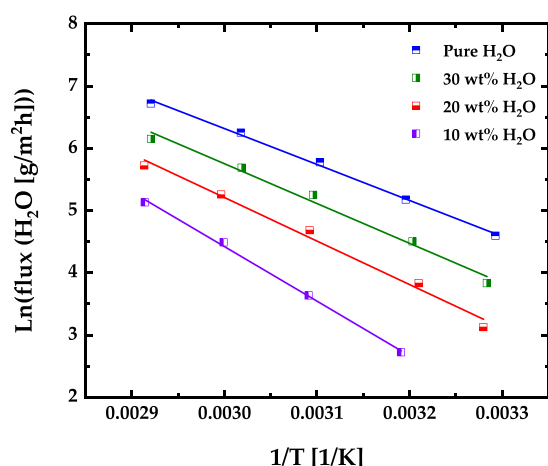
Figure 6. Natural logarithm of the H_2O flux versus the reciprocal of temperature.

the change of the driving force, which is largely dependent on both temperature and concentration. The effect on membrane permeability in nonporous membranes is usually determined from the solubility and diffusivity of the gas in the polymer matrix,[68,71] following the "solution-diffusion" mechanism when assuming a negligible concentration polarization effect.[34] The presence of water vapor would alter the noted transport mechanism due to the polymeric membrane swelling and consequently increasing molecular diffusion across the membrane. However, the use of a highly hydrophobic glassy membrane, such as Teflon AF2400 in this study, where the swelling is not the main concern, would allow the solution-diffusion mechanism despite the presence of water in the separation system.

In a pervaporation process, the calculation of the permeability coefficient requires an accurate estimation of the feed side and downside temperature to identify the real driving force of the permeation process. In vacuum pervaporation, determining the partial pressure in the downside is straightforward since the total pressure is known.[34] However, in a thermally driven TPV process, one should take a wise precaution to determine the right partial pressure in the permeate side when an air gap is present. Several works have been reported regarding the separation of binary components by TPV.[35,36,72] However, due to difficulties in experimentally determining the average temperature of the air

gap, the temperature used for the calculation of the partial pressure in the air gap is not clearly reported. In the present work, the water permeance of the membrane was estimated using both the average temperature at the condensing plate (by experiments) and the average temperature of the air gap (by simulation). The condensing plate temperature was assumed to equal to the average temperature of the cooling liquid in the inlet and outlet streams. The air-gap space was at the temperature of the condensing plate; therefore, it is saturated with water vapor, and the partial pressure of the air gap was calculated from the water vapor pressure. The membrane permeance calculated at the temperature of the condensing plate as a function of temperature and concentration is displayed in Figure 7a. The H_2O permeabilities of the membrane were calculated and are presented in Table S5, assuming negligible resistance in the porous support for small molecules. As seen from the figure, the water permeance increases slightly for all the feed concentrations and then is flattened at 50–60 °C before a drop at 70 °C (pure water, 30, and 20 wt % water). The highest value of the permeance was found around 1360 GPU at 60 °C for pure water. The permeance in the case of pure water seems to be stable in the entire temperature range. The permeance deviation for 30 wt % water feed solution is in the range of 100 GPU. The stable permeance at variable temperature is an indication for the equal increment in the flux and driving force for each experiment. Moreover, the H_2O permeability of pure water starts from ~2000 Barrer at 30 °C and fluctuates around 2050 Barrer for all of the feed temperatures. A similar trend is observed for 30 and 20 wt % water solutions. According to a producer,[54] at room temperature, the H_2O permeability of Teflon AF2400 is around 4000 Barrer. However, the producer did not provide detailed information on the experiment conditions and film preparation method. Ansaloni et al. measured the H_2O permeability of a self-standing Teflon AF2400 membrane in a vacuum pervaporation module at various temperatures,[54] and its H_2O permeability was around 3900 Barrer at room temperature. It was also found that the water permeability of the membrane shows a downward trend with increasing temperature. Dalane et al. reported the water permeability of about 2800 Barrer at 30 °C in a vacuum pervaporation study, but for a composite Teflon AF2400/Polypropylene membrane,[39] surprisingly, it showed a downward trend with increasing temperature.

The difference in the intrinsic membrane permeation results obtained in this work and between the literature values can be
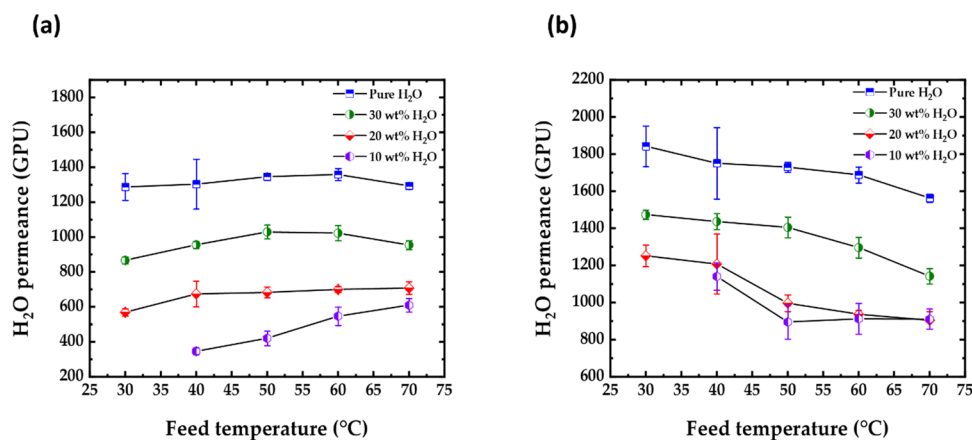
Figure 7. H_2O permeance in the AF2400/PP membrane as a function of feed temperature and concentration. (a) The air-gap partial pressure was calculated at the temperature of the condensing plate, and (b) the air-gap partial pressure was calculated at the average temperature of the air gap.
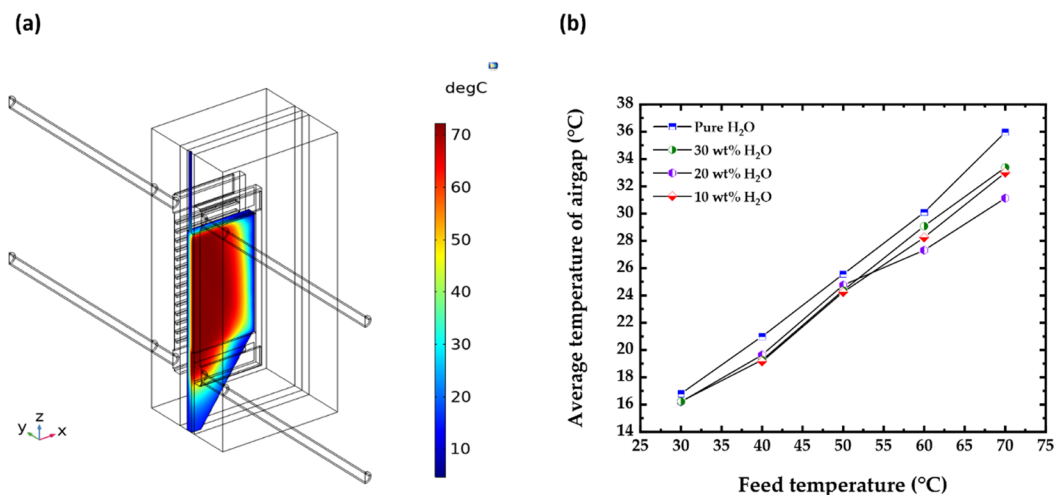
Figure 8. (a) Simulated 3D temperature profile in the air gap and (b) the simulated average temperature of the air gap as a function of feed temperature and concentration

related to the difficulties in accurately measuring the temperature within the air gap. Therefore, in this work, a 3D simulation has been employed over the entire membrane module to estimate the average temperature of the air gap to minimize the uncertainty. Another solution is to use simulation tools to find the temperature profile in the boundary layer in the air gap close to the membrane phase. However, the calculation of partial pressure of water in the boundary layer according to the obtained temperature profile requires precise values of relative humidity at the temperature of the boundary layer in the air gap. Figure 8a shows the overall 3D-simulated temperature profile of the air gap for the 30 wt % water solution at 70 °C, as an example. The temperature profile in the air gap reveals a sharp temperature drop within the 5 mm gap between the hot surface of the membrane (around 68 °C) and the cooling plate (about 4 °C).

The average temperature value of the air-gap domain was derived from the simulation study by integrating the temperature over the volume of the air gap and plotted as a function of the feed solution temperature and concentration (Figure 8b). It is evident to claim that the air-gap temperature increases as the feed temperature increases. However, the larger temperature drop between the feed solution and the average temperature of the air gap was obtained at a higher feed temperature. The highest air-gap temperature (>30 °C) was estimated for the feed solutions with an inlet temperature of about 70 °C, whereas the lowest air-gap temperature (16.8 °C) was obtained for the 30 °C case. The general trend of the air-gap temperature as a function of the feed concentration shows that the air-gap temperature is slightly higher for pure water and reduces as the concentration of TEG increases in the feed solution. The negligible effect of concentration on the air-gap temperature is due to the difference in the thermal conductivity and heat capacity of the solution and the evaporation enthalpy in the gap, which is dependent on the water flux value. It should be noted that the variation in the air-gap temperature seen from the figure for the concentrated feed solutions could be attributed to the variation in the measured inlet temperature, temperature drop along the membrane, and experimental and simulation errors.

The corrected air-gap temperature was used for the calculations of partial pressures in the permeate side, and the water permeances were re-evaluated and plotted as a function of feed concentration and temperature (Figure 7b). The higher

average temperature obtained for the air gap reduced the driving force value present in the permeation calculation, therefore increasing the H_2O permeance values; thus, a downward trend was observed, similar to that in the literature. The obtained H_2O permeabilities (Table S5 in the Supporting Information) were in good agreement with the reported values by Dalane et al.[39] Compared to the H_2O permeability reported by the producer and Ansaloni et al.[54] (3900−4000 Barrer at 25 °C for self-standing membranes), a 10−15% permeability drop was observed (3000 Barrer at 30 °C), which could be attributed to the variation in the thickness and resistance in the porous polypropylene (43 nm pore size and 41% porosity). In addition, the casting method and annealing history in membrane preparation were also reported to be possible reasons for the differences in the permeability values.[73]

As seen from the figure, the water permeance of around 1850 GPU was measured for the pure water at 30 °C, and it reduces to about 1570 GPU when the feed temperature increases to 70 °C. A similar trend was observed for all of the experiments, indicating that the enhancement of the flux is smaller than the driving force increment as temperature increases. Despite the hydrophobic nature of the polymer, the permeability of the high free volume glassy Teflon AF2400 is dominated by solubility, where the effect of temperature on the sorption coefficient is more pronounced than the temperature effect on the diffusion coefficient.[39,54] The effect of the temperature on permeability is attributed to the very small activation energy of diffusion compared to the enthalpy of sorption.[10,49,74] A similar trend is observed in microporous materials, Teflon AF2400 and PTMSP, for small molecules such as CO_2. The diffusive jump for small molecules is not hindered by the glassy nature of the polymer due to higher free volume, and for more condensable gases than CO_2, the solubility is affected to a larger extent compared to diffusivity in large free volumes.

An additional permeance drop was determined where the binary H_2O/TEG mixture was used as the feed solution. The H_2O permeances of 1437, 1208, and 1141 GPU were measured at 40 °C and reduced to the values of 1142, 904, and 911 GPU at 70 °C, for 30, 20 and 10 wt % water, respectively. The permeance drop is mainly attributed to the competitive adsorption, and also, the calculation simplifications where the additional resistance in the liquid boundary layer and viscous
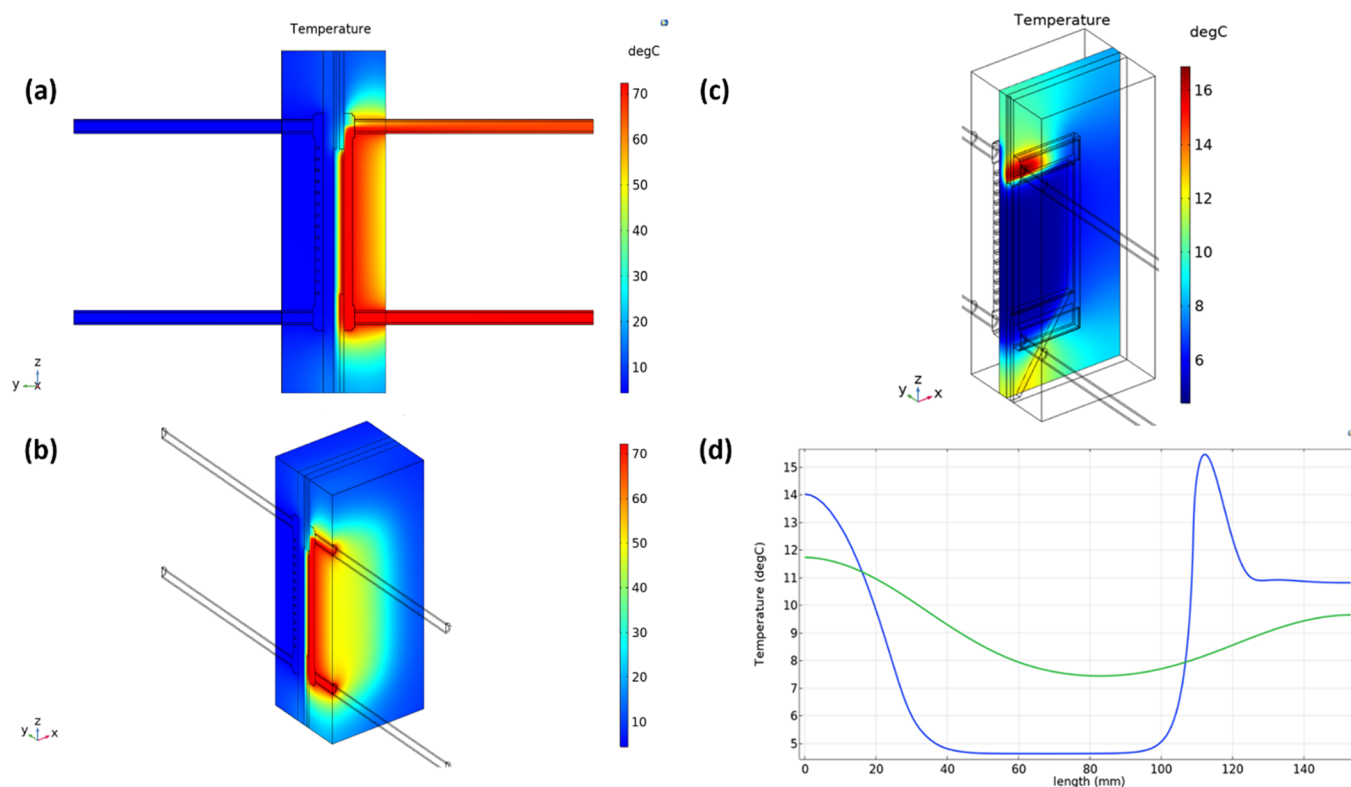
Figure 9. Temperature profiles in the TPV membrane module: (a) 2D cross-sectional image of the temperature profile of the feed fluid and channel, (b) 3D image of the temperature profile of the feed fluid and channel, (c) 3D temperature profile of the condensing plate, and (d) 1D temperature profile of the condensing plate surface in the air gap (the blue line stands for the axial centerline (at $x = 0$) of the module and the green line stands for the axial edge of the condensing plate at x = width of the module).

TEG solution at higher TEG concentrations are against the easy transport of the water.

4.4. Temperature Profile in the Membrane Module. The temperature profiles in the membrane module are presented for all domains and boundaries in Figure 9. The temperature drops along the membrane in the TPV process, and the heat loss necessitates the study of the temperature profiles in the membrane module. The importance of investigating the temperature profile in a non-isothermal TPV process stems from the fact that the water flux is a function of temperature, and it couples mass transfer with the heat transfer. The flux varies at different locations of the module, and the concentrations of the components, therefore, undergo changes due to variation in temperature at different coordinates. The effect of concentration–temperature dependency on the performance will be strong and more pronounced in a large-scale process, which should not be oversimplified by a process designer.

Figure 9 illustrates the temperature profile in the entire module in 2D and 3D views simulated for 30 wt % water solution at about 70 °C. As seen from the figures, the feed temperature undergoes a temperature drop for all experiments. The simulated temperature in the outlet feed stream is in good agreement with the experimentally measured outlet temperature data of the feed solution (Table S4). Similarly, a good agreement was also obtained for the temperature of the outlet cooling liquid. The temperature profile along the membrane shows that the use of plexiglass has successfully prevented the heat loss from/to external convection. The module body temperature was dominated by the coolant temperature initially set before feeding the solution.

The condensing plates are an important domain in the TPV process to ensure the maximum driving force for separation (Figure 9c). The use of stainless steel improves the heat transfer between the cooling liquid and the air gap. As seen from the figure, the regions on the plate facing the gas phase of the air gap have the lowest temperature close to the cooling liquid temperature, and the regions on the condensing plate that was in direct contact with the metallic framework of the air gap on the upside and downside were affected by the hot feed temperature in the entrance and exit of the feed channel. Figure 9d displays the 1D distribution of the temperature on the surface of the condensing plate facing the entire air gap. It is evident that the highest temperature drop occurs in the axial centerline of the cooling plate (blue line), and the temperature is kept at its lowest, covering the entire gas phase of the air gap. The temperature sharply increases in the axial centerline of the module at the point where the air-gap metallic frameworks are located between the condensing plate and the hot temperature in the exit of the feed channel. On the axial edge of the condensing plate (green line), however, the temperature drop is not significant compared to the centerline due to the presence of natural convection. The temperature profile on the condensing plate inside the air gap ensures the good design of the membrane module. The 1D-simulated temperature profiles indicate that the energy transfer is limited in the air gap due to the heat resistance layer provided by the stagnant air. This valuable information would further help to improve and optimize the module design for large-scale applications.

The TPV experiments were performed in the laboratory at an average temperature of 23 °C. The heat flux distribution around the surfaces is presented in the Supporting Information (Figure

S6). It should be noted that subsea facilities are insulated, where cross heaters are used to keep the whole process at a designed temperature, such as around 30 °C, which is the temperature of the closed loop.[5,10]

4.5. Water Concentration Profiles and Their Effects on Water Flux. The distribution of the water concentration in the feed channel and water vapor in the air gap was investigated. The mass transfer mechanism in the feed channel is governed by convection and diffusion in bulk followed by diffusion in the liquid boundary layer and diffusion in the membrane phase (eq S.23 in the Supporting Information). The permeated water evaporates from the membrane surface and then diffuses through the stagnant air gap, condensing finally on the cooling plate. Figure 10a presents the cross-sectional mass fraction
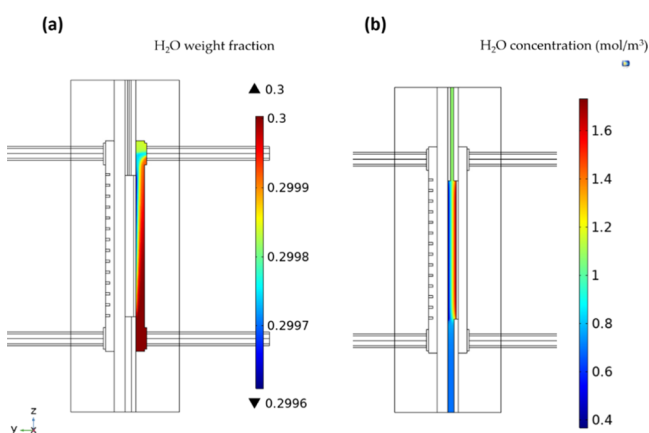

Figure 10. (a) 2D H_2O mass fraction profile of the water in the center of the membrane module in the feed channel and (b) the 2D concentration profile of the water in the air gap.

profile in the center of the membrane module (symmetry condition) on the feed side. As seen from the figure, the water mass fraction reduces as the fluid flows forward, and the TEG concentration starts to grow and accumulate axially in the vicinity of the membrane surface. The rich-TEG boundary layer

could be an indication of the well-known "concentration polarization" phenomenon induced by the temperature gradient across the membrane, which is frequently reported in membrane pervaporation. The undesired concentration polarization creates an additional mass transfer resistance toward water, competing with the membrane resistance. Despite the negligible concentration drop in the membrane module for a small area, this study shows that the presence of a TEG-rich boundary layer would be a critical issue for scaling-up the TPV process for TEG regeneration; a larger concentration drop is expected for a large-scale membrane module. The installation of a turbulence promoter in the feed channel may benefit the mass distribution in large-scale modules, as it prevents the formation of dead zones close to the walls, improves back mixing, and also increases the residence time of the fluid on the membrane surface. It should also be noted that the negligible concentration drops along the membrane ensure a small concentration change in the feed liquid reservoir during the operating time in the present experimental work.

Figure 10b illustrates the water vapor concentration profile inside the air gap. The maximum concentration of water around 1.7 mol/m^3 was achieved in the air gap close to the membrane surface for 30 wt % water feed solution at 70 °C. The gradient of the concentration is visible, and the lowest value of about 0.4 mol/m^3 was measured on the condensing plate. The concentration of the water on the condensing plate was calculated from the Antoine model. The average concentration of the air gap is presented for all of the experiments in Table S4. It is evident to claim that a higher concentration is obtained at a higher water flux permeating through the membrane, which is in the case of pure water in this study.

To further verify the temperature model and validate it with experimental data, the flux distribution on a hypothetical cut plane located at a 1 μm distance from the membrane inside the air gap was evaluated and illustrated in Figure 11. The flux model is a temperature-dependent model. The average of the flux vectors was calculated. The good agreement between the experimental flux and the estimated average flux for each experiment reveals the high accuracy of the temperature profile
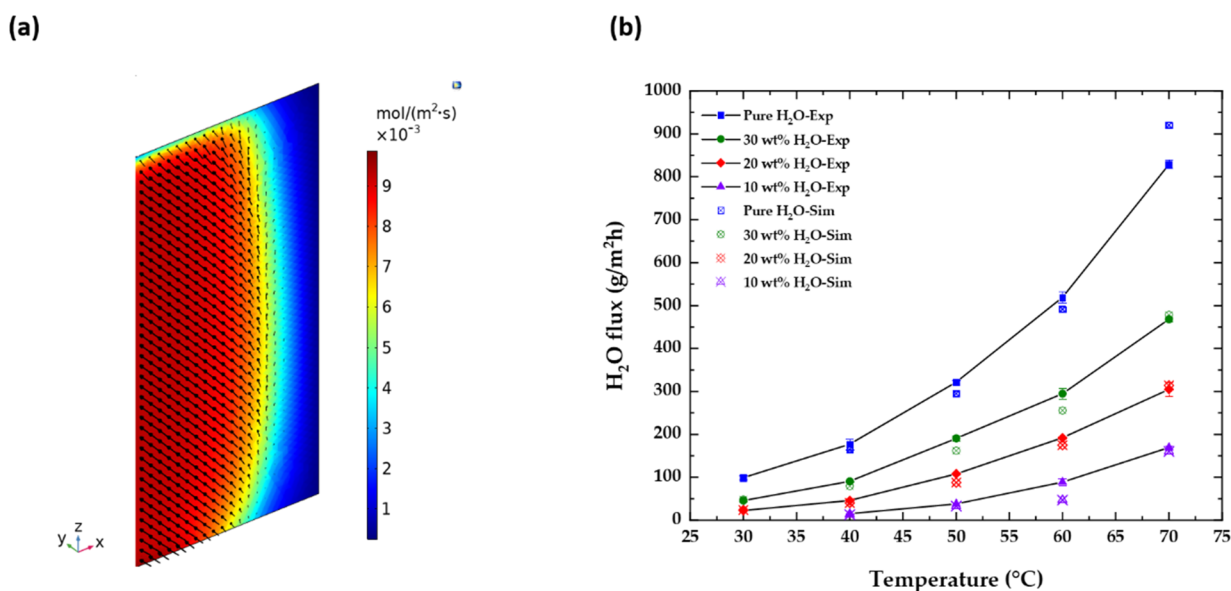
Figure 11. (a) Distribution of the flux on a hypothetical cut plane placed at 1 μm distant from the membrane in the air gap, and (b) H_2O flux as a function of temperature; filled symbols are experimental data, and crossed symbols are simulated data.

on the membrane surface. The highest values of the flux transported across the membrane occur in the regions close to the center of the module (axial centerline) due to the higher temperatures compared to the edges. The simulated water fluxes on the cut plane (average) plotted against the experimental data for each experiment are presented in Figure 11b, showing excellent agreement with the experimental results. A few minor differences could be due to the errors in the temperature gradient on the membrane surface, the assumptions for the probable liquid formation on the condensing plate, and from the regressed model of experimental flux data used as the boundary condition.

5. CONCLUSIONS

The present work developed a TPV process for TEG regeneration in a closed absorption/desorption loop for subsea natural gas dehydration. The Teflon AF2400 membrane was found to be a promising candidate for the TPV process due to its high water flux and excellent durability in TEG. The separation performance of the Teflon AF2400 confirms that the sorption is the dominating transport mechanism, and a higher temperature ensures a higher flux at the expense of the separation factor.

The effect of operating process conditions on the separation performance of the process and membrane material was experimentally evaluated for the first time. The entire membrane geometry was studied by 3D CFD mathematical simulation. The driving force was corrected according to the simulated average temperature of the air gap to fit with the experimental data of membrane permeance and permeabilities; the simulation results provided better vision to determine the "concentration-polarization" phenomenon induced by temperature gradients.

High separation factors were obtained for all feed solution concentrations at the studied operating temperatures, out-performing the VLE-based processes. A separation factor of above 128,000 for the feed containing 30 wt % water at 30 °C, which is higher than the VLE curve under similar conditions, indicates that the membrane provides additional positive selectivity toward H_2O. A water mole fraction of above 99.98% in the permeate was obtained, which would allow discharging the removed water to the seawater.

The temperature profile on the condensing plate facing the air gap reveals that the energy transfer from the hot fluid to the cold fluid is limited by the resistance of the air in the air-gap space. Moreover, the highest temperature drop between the feed solution and the average temperature of the air gap was found for the solution at 70 °C. A good agreement was observed between experimental and simulation for the outlet temperatures and water flux, validating the simulation study. The corrected permeabilities based on the simulated average temperature of the air gap were in good accordance with the reported literature data.

■ ASSOCIATED CONTENT

Ⓢ Supporting Information

The Supporting Information is available free of charge at https://pubs.acs.org/doi/10.1021/acs.iecr.1c00266.

> Details of model development and computational methods, module design, domains, and dimensions; supplementary figures and tables on the module and mesh generation, flow and operating parameters, permeabilities, activity coefficients, temperature profile, and validation parameters (PDF)

■ AUTHOR INFORMATION

Corresponding Authors

Magne Hillestad — *Department of Chemical Engineering, Norwegian University of Science and Technology (NTNU), Trondheim N-7491, Norway*; Email: magne.hillestad@ntnu.no

Liyuan Deng — *Department of Chemical Engineering, Norwegian University of Science and Technology (NTNU), Trondheim N-7491, Norway*; ⓘ orcid.org/0000-0003-4785-4620; Email: liyuan.deng@ntnu.no

Authors

Mahdi Ahmadi — *Department of Chemical Engineering, Norwegian University of Science and Technology (NTNU), Trondheim N-7491, Norway*; ⓘ orcid.org/0000-0002-5760-4134

Luca Ansaloni — *Department of Sustainable Energy Technology, SINTEF Industry, Oslo 0373, Norway*; ⓘ orcid.org/0000-0002-4930-0253

Complete contact information is available at:
https://pubs.acs.org/10.1021/acs.iecr.1c00266

Notes

The authors declare no competing financial interest.

■ ACKNOWLEDGMENTS

■ NOMENCLATURE

A_m	membrane area (m^2)
A, B, C	constants
$I_{H_2O}, S_{H_2O}, A_{TEG}, S_{TEG}$	Nakanishi parameters
C_i	concentration of component i (mol/m^3)
C_p	heat capacity of the fluid (J/kg·K)
D_i^f	Fickian diffusion coefficient of i (m^2/s)
D_{ij}^f	Fickian diffusion coefficient of i in j (m^2/s)
D_i^T	thermal diffusion of component i (m^2/s)
$D_{H_2O/air}$	diffusion of H_2O in air (m^2/s)
$D_{H_2O/TEG}$	diffusion of H_2O in TEG (m^2/s)
E_j	activation energy (j/mol)
F	body force (N)
g	gravitational acceleration (m/s^2)
h	convective heat transfer coefficient (W/(m^2·K))
H_f	height of the feed channel (m), in the x direction
J	molar flux (mol/m^2·s)
J_i	molar flux of component i (mol/m^2·s)
j	mass flux (g/m^2·h)
j_i	mass flux of component i (g/m^2·h)
j_0	Pre-exponential factor (g/m^2·h)

l	membrane dense layer thickness (m)
L_f	length of the feed channel in the z direction (m)
Mw_i	molecular weight of component i (kg/kmol)
M_n	mean molar mass of components (kg/kmol)
M_{tot}	total mass (g)
p	pressure (Pa)
p_T	total pressure in the air gap (atmospheric pressure) (cmHg)
$p_i^{sat,f}$	vapor pressure (cmHg)
$P_{AF2400,i}$	permeance (GPU)
$p_{AF2400,i}$	permeability (Barrer)
Pr	Prandtl number
Q	heat source (W/m^3)
q	conductive heat flux (J/m^2·s)
R	gas constant (J/mol·K)
Ra	Rayleigh number
R_i	inner radii of pipes (m)
R_o	outer radii of pipes (m)
r_i''	reaction term (mol/m^3·s)
r	radial coordinate
T	temperature (K in models/°C in tables)
T_r	residual temperature
T_c	critical temperature (k)
T_{ext}	external temperature (k in models/°C in tables)
t	time (h)
w_i	mass fraction of component i in the liquid phase
W_f	width of the feed channel in y direction (m)
x_i	mole fraction of component i in the liquid phase
y_i	mole fraction of component i in the vapor/gas phase
x,y,z	Cartesian coordinate

Greek Letters

α	derivative from the Gibbs−Duhem equation
μ_{TEG}	viscosity (cp) in the Nakanishi model
$\mu_{TEG/H2O}$	viscosity of TEG/H$_2$O (Kg/ms)
γ_i	activity coefficient of the ith component
β	separation factor
∇	gradient operator
ρ	density (kg/m^3)
ρ_{TEG}	density of TEG/H$_2$O (kg/m^3)
$\nu\ (\nu_z, \nu_x, \nu_y,$ and $\nu_r)$	velocity vector (m/s)
τ	stress tensor (kg/ms^2)
∇p	pressure gradient (Pa)
$\lambda_{f,c}$	thermal conductivity (W/m·K)
$\lambda_{H2O/TEG}$	thermal conductivity of TEG/H$_2$O (W/m·K)
ω_i	mass fraction of the ith component
ΔH_{evp}	enthalpy of evaporation (J/mol)
Ω_γ	constant

Superscripts, Subscripts, and Acronyms

2D	two dimensional
3D	three dimensional
f, c, w, t	feed, cooling fluid ,wall, and tube, respectively.
ss, tube	stainless steel and tube
f, inlet	feed and inlet
c, inlet	coolant and inlet
m	membrane
AG	air gap
FEM	finite element method
evp	evaporation

■ REFERENCES

(1) Dalane, K.; Dai, Z.; Mogseth, G.; Hillestad, M.; Deng, L. Potential Applications of Membrane Separation for Subsea Natural Gas Processing: A Review. *J. Nat. Gas Sci. Eng.* **2017**, *39*, 101−117. Elsevier: B.V. March 1,

(2) Albuquerque, F. A.; Vianna, F. L. V; Alves, R. P.; Kuchpil, C.; Morais, M. G. G.; Orlowski, R. T. C.; Moraes, C. A. C.; RIBEIRO, O. *Subsea Processing Systems: Future Vision; Society of Petroleum Engineers (SPE)*; 2013. DOI: 10.4043/24161-ms.

(3) Ruud, T.; Idrac, A.; McKenzie, L. J.; Hoy, S. H. All Subsea: A Vision for the Future of Subsea Processing. In *Proceedings of the Annual Offshore Technology Conference*; Offshore Technology Conference: 2015; Vol. 2, pp. 1008−1025. DOI: 10.4043/25735-ms.

(4) Parks, D.; Pack, D. Design Concept for Implementation of a Novel Subsea Gas Dehydration Process for a Gas/Condensate Well. *J. Pet. Sci. Eng.* **2013**, *109*, 18−25.

(5) Dalane, K.; Hillestad, M.; Deng, L. Subsea Natural Gas Dehydration with Membrane Processes: Simulation and Process Optimization. *Chem. Eng. Res. Des.* **2019**, *142*, 257−267.

(6) Mokhatab, S.; Poe, W. A.; Speight, J. G. *Handbook of Natural Gas Transmission and Processing*; Elsevier Inc.: 2006. DOI: 10.1016/B978-0-7506-7776-9.X5000-3.

(7) Netusil, M.; Ditl, P. Comparison of Three Methods for Natural Gas Dehydration. *J. Nat. Gas Chem.* **2011**, *20*, 471−476.

(8) Anyadiegwu, C. I. C.; Kerunwa, A.; Oviawele, P. Natural Gas Dehydration Using Triethylene Glycol (TEG). *Pet. Coal* **2014**, *56*, 407−417.

(9) Hubbard, R. A. Recent Developments in Gas Dehydration and Hydrate Inhibition. In *SPE Gas Technology Symposium*; Society of Petroleum Engineers: 1991. DOI: 10.2118/21507-MS.

(10) Ahmadi, M.; Lindbråthen, A.; Hillestad, M.; Deng, L. Subsea Natural Gas Dehydration in a Membrane Contactor with Turbulence Promoter: An Experimental and Modeling Study. *Chem. Eng. J.* **2021**, 126535.

(11) Xu, Y.; Chen, C.; Zhang, P.; Sun, B.; Li, J. Pervaporation Properties of Polyimide Membranes for Separation of Ethanol + Water Mixtures. *J. Chem. Eng. Data* **2006**, *51*, 1841−1845.

(12) Yadav, A.; Lind, M. L.; Ma, X.; Lin, Y. S. Nanocomposite Silicalite-1/Polydimethylsiloxane Membranes for Pervaporation of Ethanol from Dilute Aqueous Solutions. *Ind. Eng. Chem. Res.* **2013**, *52*, 5207−5212.

(13) Zhu, T.; Yu, X.; Yi, M.; Wang, Y. Facile Covalent Crosslinking of Zeolitic Imidazolate Framework/Polydimethylsiloxane Mixed Matrix Membrane for Enhanced Ethanol/Water Separation Performance. *ACS Sustainable Chem. Eng.* **2020**, *8*, 12664−12676.

(14) Luyben, W. L. Control of a Column/Pervaporation Process for Separating the Ethanol/Water Azeotrope. *Ind. Eng. Chem. Res.* **2009**, *48*, 3484−3495.

(15) Xiangli, F.; Chen, Y.; Jin, W.; Xu, N. Polydimethylsiloxane (PDMS)/Ceramic Composite Membrane with High Flux for Pervaporation of Ethanol-Water Mixtures. *Ind. Eng. Chem. Res.* **2007**, *46*, 2224−2230.

(16) Aguilar-Valencia, D. M.; Gómez-García, M. Á.; Fontalvo, J. Effect of PH, CO$_2$, and High Glucose Concentrations on Polydimethylsiloxane Pervaporation Membranes for Ethanol Removal. *Ind. Eng. Chem. Res.* **2012**, *51*, 9328−9334.

(17) Claessens, B.; Dubois, N.; Lefevere, J.; Mullens, S.; Cousin-Saint-Remi, J.; Denayer, J. F. M. 3D-Printed ZIF-8 Monoliths for Biobutanol Recovery. *Ind. Eng. Chem. Res.* **2020**, *59*, 8813−8824.

(18) Kamtsikakis, A.; McBride, S.; Zoppe, J. O.; Weder, C. Cellulose Nanofiber Nanocomposite Pervaporation Membranes for Ethanol Recovery. *ACS Appl. Nano Mater.* **2021**, *4*, 568−579.

(19) Cheng, C.; Liu, F.; Yang, H. K.; Xiao, K.; Xue, C.; Yang, S. T. High-Performancen-Butanol Recovery from Aqueous Solution by Pervaporation with a PDMS Mixed Matrix Membrane Filled with Zeolite. *Ind. Eng. Chem. Res.* **2020**, *59*, 7777−7786.

(20) Cai, W.; Cheng, X.; Chen, X.; Li, J.; Pei, J. Poly(Vinyl Alcohol)-Modified Membranes by Ti3C2Txfor Ethanol Dehydration via Pervaporation. *ACS Omega* **2020**, *5*, 6277−6287.

(21) Zou, C.; Lin, L. C. Potential and Design of Zeolite Nanosheets as Pervaporation Membranes for Ethanol Extraction. *Ind. Eng. Chem. Res.* **2020**, *59*, 12845−12854.

(22) Li, G.; Ma, S.; Ye, F.; Zhou, L.; Wang, Y.; Lang, X.; Fan, S. Robust ZSM-5 Membranes for Efficient Bio-Oil Dehydration: Transport Mechanism and Its Implication on Structural Tuning. *Ind. Eng. Chem. Res.* **2021**, *60*, 1799−1807.

(23) Huang, R. Y. M.; Moon, G. Y.; Pal, R. Ethylene Propylene Diene Monomer (EPDM) Membranes for the Pervaporation Separation of Aroma Compound from Water. *Ind. Eng. Chem. Res.* **2002**, *41*, 531−537.

(24) Okamoto, K.-i.; Kita, H.; Horii, K.; Tanaka, K.; Kondo, M. Zeolite NaA Membrane: Preparation, Single-Gas Permeation, and Pervaporation and Vapor Permeation of Water/Organic Liquid Mixtures. *Ind. Eng. Chem. Res.* **2001**, *40*, 163−175.

(25) Hir, M. L.; Magne, A.; Clair, T.; Carretier, E.; Moulin, P. Solvent Regeneration in Complex Mixture Using Pervaporation. *Org. Process Res. Dev.* **2021**, 469.

(26) He, Q.-P.; Zou, Y.; Wang, P.-F.; Dou, X. MFI-Type Zeolite Membranes for Pervaporation Separation of Dichlorobenzene Isomers. *ACS Omega* **2021**, 8456.

(27) Rao, P. S.; Sridhar, S.; Ming, Y. W.; Krishnaiah, A. Pervaporative Separation of Ethylene Glycol/Water Mixtures by Using Cross-Linked Chitosan Membranes. *Ind. Eng. Chem. Res.* **2007**, *46*, 2155−2163.

(28) Hyder, M. N.; Huang, R. Y. M.; Chen, P. Composite Poly(Vinyl Alcohol)-Poly(Sulfone) Membranes Crosslinked by Trimesoyl Chloride: Characterization and Dehydration of Ethylene Glycol-Water Mixtures. *J. Memb. Sci.* **2009**, *326*, 363−371.

(29) Spitzen, J. W. F. *Pervaporation: Membranes and Models for the Dehydration of Ethanol*; October 1988.

(30) Cheng, X.; Pan, F.; Wang, M.; Li, W.; Song, Y.; Liu, G.; Yang, H.; Gao, B.; Wu, H.; Jiang, Z. Hybrid Membranes for Pervaporation Separations. *J. Membr. Sci.* **2017**, *541*, 329−346.

(31) Feng, X.; Huang, R. Y. M. Liquid Separation by Membrane Pervaporation: A Review. *Ind. Eng. Chem. Res.* **1997**, *36*, 1048−1066.

(32) Wang, Y.; Chung, T. S.; Neo, B. W.; Gruender, M. Processing and Engineering of Pervaporation Dehydration of Ethylene Glycol via Dual-Layer Polybenzimidazole (PBI)/Polyetherimide (PEI) Membranes. *J. Memb. Sci.* **2011**, *378*, 339−350.

(33) Baker, R. W. *Membrane Technology and Applications*; John Wiley & Sons: 2012. DOI: 10.1002/9781118359686.

(34) Baker, R. W.; Wijmans, J. G.; Huang, Y. Permeability, Permeance and Selectivity: A Preferred Way of Reporting Pervaporation Performance Data. *J. Membr. Sci.* **2010**, *348*, 346−352.

(35) Borisov, I. L.; Golubev, G. S.; Vasilevsky, V. P.; Volkov, A. V.; Volkov, V. V. Novel Hybrid Process for Bio-Butanol Recovery: Thermopervaporation with Porous Condenser Assisted by Phase Separation. *J. Membr. Sci.* **2017**, *523*, 291−300.

(36) Borisov, I. L.; Volkov, V. V. Thermopervaporation Concept for Biobutanol Recovery: The Effect of Process Parameters. *Sep. Purif. Technol.* **2015**, *146*, 33−41.

(37) Aptel, P.; Challard, N.; Cuny, J.; Neel, J. Application of the Pervaporation Process to Separate Azeotropic Mixtures. *J. Membr. Sci.* **1976**, *1*, 271−287.

(38) Wang, Y.; Gruender, M.; Chung, T. S. Pervaporation Dehydration of Ethylene Glycol through Polybenzimidazole (PBI)-Based Membranes. 1. Membrane Fabrication. *J. Membr. Sci.* **2010**, *363*, 149−159.

(39) Dalane, K.; Josefsen, N. T.; Ansaloni, L.; Hillestad, M.; Deng, L. Thermopervaporation for Regeneration of Triethylene Glycol (TEG):Experimental and Model Development. *J. Membr. Sci.* **2019**, *588*, 117205.

(40) Golubev, G. S.; Podtynnikov, I. A.; Balynin, A. V.; Borisov, I. L. Triethylene Glycol Dehydration by Thermopervaporation. In *Key Engineering Materials*; Trans Tech Publications Ltd: 2020; Vol. *869* KEM, pp 182−189. DOI: 10.4028/www.scientific.net/KEM.869.182.

(41) Hu, C.; Li, B.; Guo, R.; Wu, H.; Jiang, Z. Pervaporation Performance of Chitosan-Poly(Acrylic Acid) Polyelectrolyte Complex Membranes for Dehydration of Ethylene Glycol Aqueous Solution. *Sep. Purif. Technol.* **2007**, *55*, 327−334.

(42) Hu, C.; Guo, R.; Li, B.; Ma, X.; Wu, H.; Jiang, Z. Development of Novel Mordenite-Filled Chitosan-Poly(Acrylic Acid) Polyelectrolyte Complex Membranes for Pervaporation Dehydration of Ethylene Glycol Aqueous Solution. *J. Memb. Sci.* **2007**, *293*, 142−150.

(43) Guo, R.; Hu, C.; Pan, F.; Wu, H.; Jiang, Z. PVA-GPTMS/TEOS Hybrid Pervaporation Membrane for Dehydration of Ethylene Glycol Aqueous Solution. *J. Memb. Sci.* **2006**, *281*, 454−462.

(44) Hyder, M. N.; Chen, P. Pervaporation Dehydration of Ethylene Glycol with Chitosan-Poly(Vinyl Alcohol) Blend Membranes: Effect of CS-PVA Blending Ratios☆. *J. Membr. Sci.* **2009**, *340*, 171−180.

(45) Guo, R.; Hu, C.; Li, B.; Jiang, Z. Pervaporation Separation of Ethylene Glycol/Water Mixtures through Surface Crosslinked PVA Membranes: Coupling Effect and Separation Performance Analysis. *J. Memb. Sci.* **2007**, *289*, 191−198.

(46) Rezakazemi, M.; Shahverdi, M.; Shirazian, S.; Mohammadi, T.; Pak, A. CFD Simulation of Water Removal from Water/Ethylene Glycol Mixtures by Pervaporation. *Chem. Eng. J.* **2011**, *168*, 60−67.

(47) Yong Nam, S.; Moo Lee, Y. Pervaporation of Ethylene Glycol-Water Mixtures. I. Pervaporation Performance of Surface Crosslinked Chitosan Membranes. *J. Membr. Sci.* **1999**, *153*, 155−162.

(48) Sun, D.; Yang, P.; Sun, H. L.; Li, B. B. Preparation and Characterization of Cross-Linked Poly (Vinyl Alcohol)/Hyper-branched Polyester Membrane for the Pervaporation Dehydration of Ethylene Glycol Solution. *Eur. Polym. J.* **2015**, *62*, 155−166.

(49) Pinnau, I.; Toy, L. G. Gas and Vapor Transport Properties of Amorphous Perfluorinated Copolymer Membranes Based on 2,2-Bistrifluoromethyl-4,5-Difluoro-1,3-Dioxole/Tetrafluoroethylene. *Membr. Sci.ence* **1996**, *109*, 125−133. Elsevier B.V.,

(50) Lowry, J. H.; Mendlowitz, J. S.; Subramanian, N. S. Optical Characteristics of Teflon AF Fluoroplastic Materials. *Opt. Eng.* **1992**, *31*, 1982.

(51) Ferrari, M. C.; Galizia, M.; De Angelis, M. G.; Sarti, G. C. Gas and Vapor Transport in Mixed Matrix Membranes Based on Amorphous Teflon AF1600 and AF2400 and Fumed Silica, DOI: 10.1021/ie100242q.

(52) Smuleac, V.; Wu, J.; Nemser, S.; Majumdar, S.; Bhattacharyya, D. Novel Perfluorinated Polymer-Based Pervaporation Membranes for Separation of Solvent/Water Mixtures. *J. Memb. Sci.* **2010**, *352*, 41−49.

(53) Dalane, K.; Svendsen, H. F.; Hillestad, M.; Deng, L. Membrane Contactor for Subsea Natural Gas Dehydration: Model Development and Sensitivity Study. *J. Memb. Sci.* **2018**, *556*, 263−276.

(54) Ansaloni, L.; Rennemo, R.; Knuutila, H. K.; Deng, L. Development of Membrane Contactors Using Volatile Amine-Based Absorbents for CO2 Capture: Amine Permeation through the Membrane. *J. Memb. Sci.* **2017**, *537*, 272−282.

(55) Ansaloni, L.; Hartono, A.; Awais, M.; Knuutila, H. K.; Deng, L. CO2 Capture Using Highly Viscous Amine Blends in Non-Porous Membrane Contactors. *Chem. Eng. J.* **2019**, *359*, 1581−1591.

(56) Bondar, V. I.; Freeman, B. D.; Yampolskii, Y. P. Sorption of Gases and Vapors in an Amorphous Glassy Perfluorodioxole Copolymer. *Macromolecules* **1999**, 6163.

(57) Tokarev, A.; Friess, K.; Machkova, J.; Šipek, M.; Yampolskii, Y. Sorption and Diffusion of Organic Vapors in Amorphous Teflon AF2400. *J. Polym. Sci. Part B: Polym. Phys.* **2006**, *44*, 832.

(58) Liu, S.; Ma, L. C.; Chen, C. H.; Chen, C.; Lin, Y. S. Highly Gas Permeable, Ultrathin Teflon AF2400/Γ-Alumina Composite Hollow Fiber Membranes for Dissolved Gas Analysis. *J. Memb. Sci.* **2017**, 243.

(59) Ferrari, M. C.; Galizia, M.; De Angelis, M. G.; Sarti, G. C. Gas and Vapor Transport in Mixed Matrix Membranes Based on Amorphous Teflon AF1600 and AF2400 and Fumed Silica. *Ind. Eng. Chem. Res.* **2010**, 11920.

(60) Polyakov, A. M.; Starannikova, L. E.; Yampolskii, Y. P. Amorphous Teflons AF as Organophilic Pervaporation Materials Transport of Individual Components. *J. Membr. Sci.* **2003**, *216*, 241−256.

(61) Koter, S.; Kujawska, A.; Kujawski, W. Modeling of Transport and Separation in a Thermopervaporation Process. *J. Memb. Sci.* **2015**, *480*, 129−138.

(62) Borisov, I. L.; Volkov, V. V.; Kirsh, V. A.; Roldugin, V. I. Simulation of the Temperature-Driven Pervaporation of Dilute 1-Butanol Aqueous Mixtures through a PTMSP Membrane in a Cross-Flow Module. *Pet. Chem.* **2011**, *51*, 542−554.

(63) Parish, W. R.; Won, K.; Baltau, M. Phase Behaviour of the Triethylene Glycol-Water System and Dehydration/Regeneration Design for Extremely Low Dew Point Requirement. In *In 65 th Annual Convention of the GPSA, TX.*; 1986.

(64) Poling, B. E.; Prausnitz, J. M.; O'connell, J. P.; York, N.; San, C.; Lisbon, F.; Madrid, L.; City, M.; Delhi, M. N.; Juan, S. *The Properties of Gas and Liquids* 5th Edition McGRAW-HILL: 2001. DOI: 10.1036/0070116822.

(65) DOW Company. *Triethylene Glycol-DOW*; 2007. https://www.yumpu.com/en/document/read/6898091/triethylene-glycol-the-dow-chemical-company

(66) Coker, A. K. *Ludwig's Applied Process Design for Chemical and Petrochemical Plants*; Elsevier Inc.: 2007. DOI: 10.1016/B978-0-7506-7766-0.X5000-3.

(67) Liu, K.; Bai, P.; Bazant, M. Z.; Wang, C. A.; Li, J. A Soft Non-Porous Separator and Its Effectiveness in Stabilizing Li Metal Anodes Cycling at 10 MA Cm^{-2} Observed in Situ in a Capillary Cell. *J. Mater. Chem. A* **2017**, *5*, 4300−4307.

(68) Hu, S. Y.; Zhang, Y.; Lawless, D.; Feng, X. Composite Membranes Comprising of Polyvinylamine-Poly(Vinyl Alcohol) Incorporated with Carbon Nanotubes for Dehydration of Ethylene Glycol by Pervaporation. *J. Membr. Sci.* **2012**, *417-418*, 34−44.

(69) Shi, G. M.; Yang, T.; Chung, T. S. Polybenzimidazole (PBI)/Zeolitic Imidazolate Frameworks (ZIF-8) Mixed Matrix Membranes for Pervaporation Dehydration of Alcohols. *J. Memb. Sci.* **2012**, *415-416*, 577−586.

(70) Du, J. R.; Chakma, A.; Feng, X. Dehydration of Ethylene Glycol by Pervaporation Using Poly(N,N-Dimethylaminoethyl Methacrylate)/Polysulfone Composite Membranes. *Sep. Purif. Technol.* **2008**, *64*, 63−70.

(71) Ahmadi, M.; Janakiram, S.; Dai, Z.; Ansaloni, L.; Deng, L. Performance of Mixed Matrix Membranes Containing Porous Two-Dimensional (2D) and Three-Dimensional (3D) Fillers for CO2 Separation: A Review. *Membranes (Basel).* **2018**, *8*, 50.

(72) Kujawska, A.; Kujawski, J.; Bryjak, M.; Kujawski, W. Removal of Volatile Organic Compounds from Aqueous Solutions Applying Thermally Driven Membrane Processes. 1. Thermopervaporation. *Chem. Eng. Process. Process Intensif.* **2015**, *94*, 62−71.

(73) Scholes, C. A.; Kanehashi, S.; Stevens, G. W.; Kentish, S. E. Water Permeability and Competitive Permeation with CO2 and CH4 in Perfluorinated Polymeric Membranes. *Sep. Purif. Technol.* **2015**, *147*, 203−209.

(74) Yampolskii, Y.; Pinnau, I.; Freeman, B. D. *Materials Science of Membranes for Gas and Vapor Separation*; Yampolskii, Y., Pinnau, I., Freeman, B., Eds.; John Wiley & Sons, Ltd: Chichester, UK, 2006. DOI: 10.1002/047002903X.